Journal of Luminescence 250 (2022) 119097

Contents lists available at ScienceDirect

Journal of Luminescence

journal homepage: www.elsevier.com/locate/jlumin

Full Length Article

Covalent and noncovalent hybrids of di-amino porphyrin functionalized graphene oxide and their interaction with gold nanoparticles

Suzana M. Andrade [a,*], Vanda Vaz Serra [a], Carlos J. Bueno-Alejo [a,1], Ana Rosa Garcia [b,c], M. Fernanda N.N. Carvalho [a], Laura M. Ilharco [b], Maria Graça P.M.S. Neves [d], Sílvia M.B. Costa [a]

[a] Centro de Química Estrutural, Institute of Molecular Sciences, Instituto Superior Técnico, Universidade de Lisboa, Av. Rovisco Pais 1049 001 Lisboa, Portugal
[b] Centro de Química-Física Molecular and IBB - Institute of Bioengineering and Biosciences, Instituto Superior Tecnico, Universidade de Lisboa, 1049-001, Lisboa, Portugal
[c] Departamento de Química e Farmácia, FCT, Universidade Do Algarve, Campus de Gambelas, 8005-139, Faro, Portugal
[d] LAQV-REQUIMTE, Department of Chemistry, University of Aveiro, 3810-193 Aveiro, Portugal

ARTICLE INFO

Keywords:
Photofunctional materials
Graphene
Metal-enhanced fluorescence
Photoinduced electron transfer
Confocal fluorescence lifetime microscopy

ABSTRACT

Porphyrin functionalization of graphene oxide (GO) influenced the plasmonic effect of gold nanoparticles (AuNP). The former was achieved by modification of GO with 5,10-bis(4-aminophenyl)-15,20-diphenylporphyrin, $P(NH_2)_{2,adj}$, by noncovalent interactions as well as by covalent association, following standard chemistry. The success of the chemical functionalization of GO with $P(NH_2)_{2,adj}$, was confirmed by FTIR. Steady-state and time-resolved fluorescence showed a strong fluorescence quenching of porphyrin in the presence of GO, indicative of a photoinduced electron transfer process from porphyrin units to GO, which acts as an electron acceptor. The surface plasmon coupling effect promoted by the AuNP@GO hybrids, proved to be effective only in the case of the noncovalent hybrid, detected through the decrease of the porphyrin fluorescence lifetime and increase in the emission intensity in solution, in good agreement with FLIM results on deposited samples.

1. Introduction

Many processes central to chemistry and biology such as photosynthesis, respiration, and enzyme electrocatalysis are driven by long-range electron transfer. These natural processes have motivated the emergence of molecular electronics which, in turn, provided significant insights toward understanding and measuring charge transport events in distinct nanoarchitectures [1–3]. In this context, donor-acceptor (D–A) hybrids of porphyrinoids (such as porphyrins and phthalocyanines) and carbon-based materials (CBM), such as carbon nanotubes (CNTs) and graphene, are currently an important scientific frontier [4–6]. As individual materials, their contribution stands up in distinct fields of application. CBM and in particular graphene and its derivatives have gathered large interest due to the combination of outstanding electronic and optical properties [7] with impressive surface area and mechanical strength which impart them with a wide range of applications in science and technology, from energy conversion to sensing [8,9]. Still, it is well-known that CBM tends to aggregate due to the strong van der Waals forces. In turn, graphene oxide (GO) can be readily suspended in aqueous environments which greatly spans its application into the biological realm [10,11]. Chemical oxidation of graphite to graphene oxide (GO) results in exfoliated sheets and introduces oxygen groups along with structural defects which can be used to interact covalently or noncovalently with electron donors and/or acceptors [12–14]. In this context, porphyrinoids represent an adequate system to explore in conjugation with CBM. Porphyrins' key role in many biological processes associated with their tailor-made synthesis possibilities, potentiates their interest in research areas such as catalysis, electrochemistry, and optoelectronics [15,16]. In the recent past, both covalent and noncovalent interactions between CBM and porphyrinoids have proven to produce hybrids with novel and/or improved properties as compared to their elements [17–22].

Despite the increasing contributions involving noncovalent or covalent interactions of porphyrinoids with graphene (or with GO), the combination of these hybrids with metal nanoparticles (MNP) has received less attention [23,24]. AuNP are well known for their unique electrocatalytic activity [25,26]. These plasmonic nanostructures can also produce highly localized heat during the rapid relaxation process,

* Corresponding author.
E-mail address: suzana.andrade@tecnico.ulisboa.pt (S.M. Andrade).
[1] Present address: Department of Molecular and Cell Biology, University of Leicester, Leicester, LE1 7RH, United Kingdom.

https://doi.org/10.1016/j.jlumin.2022.119097
Received 19 March 2022; Received in revised form 18 June 2022; Accepted 22 June 2022
Available online 2 July 2022

which has led to their use as photothermal and anti-angiogenic agents [27,28]. Nonetheless, AuNP alone may suffer from the same aggregation problems as GO. Therefore, the combination of the two nanomaterials is expected to lead to more stable suspensions with potential synergistic performance. Recently, it was shown that porphyrinoids' interaction with nanoarchitectures of AuNP@GO resulted in an enhancement of the fluorophore's emission depending on the distance and orientation of the latter relative to the nanoparticles. This phenomenon of fluorescence intensity increase (together with the fluorescence lifetime decrease) of a fluorophore in the vicinity of the plasmonic nanostructure (MEF) is of considerable interest in biomedicine [29,30].

In this research contribution, we have synthesized a di-amino *para*-substituted tetraphenyl porphyrin, $P(NH_2)_{2,adj}$, which was directly coupled to GO through an amide linkage, using previously established synthetic methodologies [20,21,31], as well as noncovalently through hydrogen bonding and π−π interactions, Scheme 1. Hence, we can profit from these conjugates' interactions to produce highly dispersible sheets in aqueous solutions and explore donor-acceptor processes. The interaction of both conjugates with AuNP was followed to assess the conditions to maximize the MEF effect of such plasmonic nanostructures. Photonic properties of these hybrid materials were evaluated as regards the ground-state interaction, as well as the excited-state deactivation mechanism of both covalent and noncovalent conjugates, probed in solution and complemented with fluorescence lifetime imaging microscopy (FLIM) information on the respective deposited samples.

2. Experimental

2.1. Materials

Graphite powder (synthetic, conducting grade, −325 mesh, 99.9995% metals basis) was obtained from Alfa Aesar and sodium tetrachloroaurate (III) dihydrate (99%) from Sigma-Aldrich. The solvents dichloromethane (DCM), chloroform (CLF), acetonitrile (ACNT), and dimethylformamide (DMF) are anhydrous and were also purchased from Sigma-Aldrich. All other chemicals were obtained from commercial sources and used without further purification unless otherwise specified. Milli-Q water (DW) was used in the experiments.

2.2. Synthetic procedures

Synthesis of $P(NH_2)_{2,adj}$ – The $P(NH_2)_{2,adj}$ porphyrin was prepared according to literature procedures [32] and references therein. Briefly, a concentrated solution of 5,10,15,20 - tetraphenylporphyrin (TPP) in trifluoroacetic acid (TFA) was treated with 8.1 equiv. of sodium nitrite for 1.5 min resulting in the formation of a mixture of two isomeric di-nitrophenylporphyrins. These were then converted into the corresponding aminoporphyrins by reduction with tin(II) chloride and HCl, and separated by column chromatography. The characterization was made using NMR and mass spectrometry.

Synthesis of $P(NH_2)_{2,adj}$ – GO covalent hybrid: The synthesis of $P(NH_2)_{2,adj}$ – GO hybrid starts with the activation of the carboxylic units of GO (10 mg) by forming the correspondent acyl chloride upon addition of $SOCl_2$ (10 mL) and DMF (250 μL). The mixture was left overnight under reflux. Afterward, the reaction mixture was evaporated to remove the excess of $SOCl_2$ and the brownish solid was dispersed in dry THF containing the porphyrin (10 mg) and left at room temperature and under N_2 atmosphere for 72 h. The hybrid material ($P(NH_2)_{2,adj}$ – GO) was obtained after filtration (0.2 μm PTFE filter) and then thoroughly washed with dichloromethane (4 × 20 mL) to remove unreacted free porphyrin (until the filtrate was colorless). Finally, diethyl ether was added before drying under vacuum to obtain the required hybrid for further characterization and functionalization. The preparation of the covalent hybrid was made by dispersion of the solid in the aqueous DMF mixture (2:1 v/v) solution and left under mild stirring for 24 h at room temperature.

Preparation of $P(NH_2)_{2,adj}$+ GO noncovalent hybrid: The desired amount of GO was dispersed in an aqueous DMF mixture (2:1 v/v) solution using the ultrasonic bath for 20–30 min. Afterward, a small volume of a DMF stock solution of the porphyrin was added and the mixture was left under mild stirring for 24 h at room temperature (typical concentrations used 0.03 mg/mL of GO and 1.5 μM of porphyrin) followed by filtration to remove free porphyrin.

Adsorption of AuNP to GO and GO-$P(NH_2)_{2,adj}$: Typically, for a 50 mL

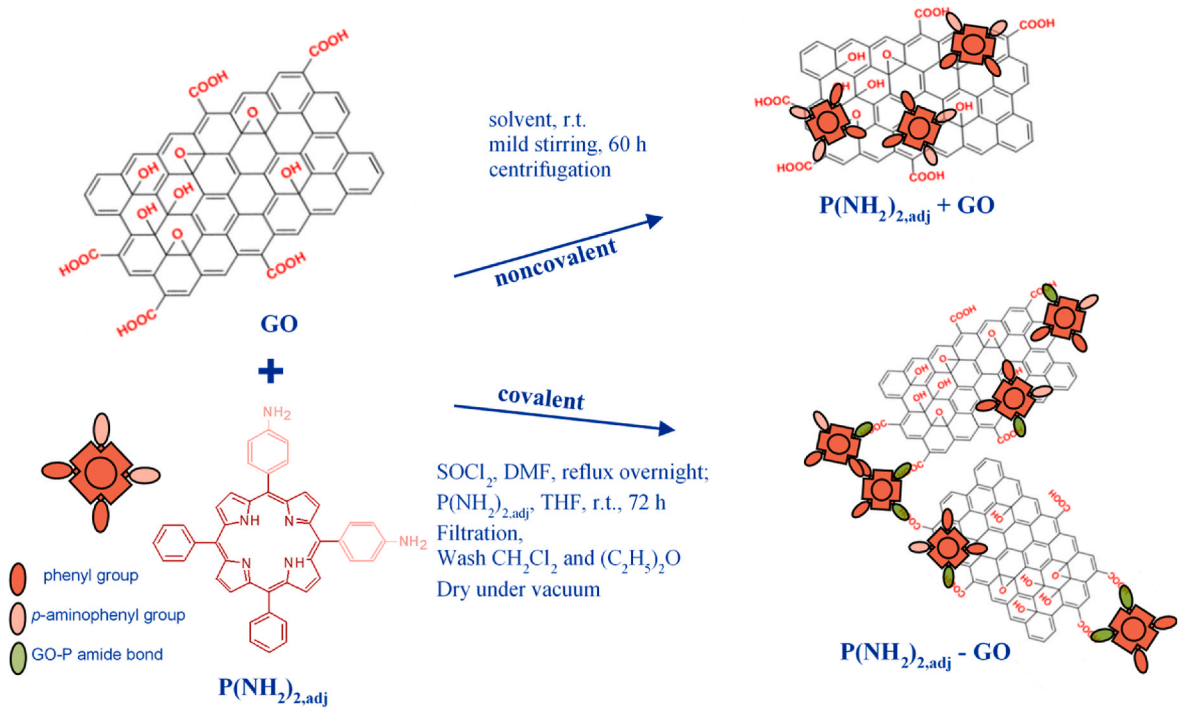

Scheme 1. Synthesis and preparation of covalent $P(NH_2)_{2,adj}$ – GO and noncovalent $P(NH_2)_{2,adj}$ + GO hybrids.

volume, 10 mg of GO were weighted and ultrapure water was added; the solution was set in the ultrasonic bath for 20–30 min and N_2-gas was bubbled through to replace the air inside the flask (this has two purposes: N_2-gas is inert and will not influence the reaction while air might do that; it makes the solution more homogeneous). Gold nanoparticles were prepared separately (see description in SI†). Afterward, 3 mL of the AuNP solution was added and put again in the ultrasonic bath, for one and a half hours. After centrifugation, the dark pellet was washed twice with Milli-Q water. The combined material of AuNP and GO was recovered, by drying it in an oven at 50 °C for at least one night. A similar procedure was undertaken for AuNP adsorption to the covalent hybrid.

2.3. Characterization techniques

Infrared spectroscopy in diffuse reflectance mode (DRIFT): The spectra were obtained with a Mattson Research Series 1 FTIR spectrometer, using a wide-band MCT detector (4000-400 cm^{-1}) and a Graseby/Specac Selector (with specular reflection blocker). The sample preparation consisted simply of grinding a mixture of KBr (Sigma-Aldrich, FTIR grade) and each sample powder. The amount of sample in the sample holder was consistent with infinite thickness and the adequate proportions KBr:sample (~4:1) were used to obtain spectral absorbance in the range of applicability of the Kubelka-Munk transformation [33]. The spectra were the ratio of 500 single beam scans of the sample to the same number of background scans for pure KBr with 4 cm^{-1} resolution.

UV–Vis Absorption and Fluorescence: UV–visible absorption or extinction spectra were recorded in a PerkinElmer Lambda 35 UV/vis spectrophotometer. Quartz cells with an optical path length of 1 cm were used. The necessary corrections for turbidity were carried out. Corrected steady-state fluorescence spectra were obtained with a SPEX® Fluorolog spectrofluorimeter (HORIBA Jobin Yvon) in an FL3-11 configuration. The time-correlated single-photon counting (TC-SPC) option on the Fluorolog spectrofluorimeter was used to obtain fluorescence decays in solution. Excitation at 372 and 445 nm was achieved using a NanoLED (fwhm <1.0 ns), at a repetition rate of 1 MHz, and the individual photons were detected by a Hamamatsu R928 PMT and stored on an IBH Data Station Hub photon counting module. The data rate was set proportional to the source repetition rate up to ~2% to avoid photon pileup artifacts. The instrumental response function was obtained with a suspension of Ludox (colloidal silica beads) in water. Alternatively, fluorescence lifetimes were obtained with the TC-SPC technique using commercial equipment Microtime 200 (PicoQuant, Berlin, Germany). Excitation was achieved using pulsed laser diode heads (405 nm; 638 nm), with varied repetition rates (10, 20, or 40 MHz). Appropriate band-pass filters were used to eliminate back-scattered light in the photomultiplier tube from PicoQuant (model PMA-182). In both cases, data analysis was performed by a deconvolution method using a non-linear least-squares fitting program, based on the Marquardt algorithm. The goodness of the fit was evaluated by the usual statistical criteria and by visual inspection of the weighted residuals distribution and the autocorrelation function.

Fluorescence Lifetime Imaging Microscopy (FLIM): FLIM was performed in the same Microtime 200 set-up and a more detailed description can be found elsewhere [34,35]. Briefly, the 638 nm pulsed diode laser was focused by a water immersion objective (60x; 1.2 NA) into the sample. Fluorescence was collected by the same microscope objective, passed through the dichroic mirror and suitable bandpass filter, and focused through a pinhole (30 μm), to reject out-of-focus light, onto a single-photon counting avalanche photodiode (PerkinElmer) whose signal was processed by a TimeHarp 200 TC-SPC PC-board (PicoQuant) working in the special Time-Tagged Time-Resolved mode which stores all relevant information for every detected photon. The average photon count rate was 0.5–1 x 10^4 counts/s. Immobilized samples for FLIM were prepared on previously cleaned and hydrophilized glass slides (30 min in freshly prepared piranha solution, H_2O_2:H_2SO_4 = 1:3) by drop-casting.

Cyclic voltammetry: The redox properties of $(P–NH_2)_{2,adj}$ were studied by cyclic voltammetry using a three compartments cell, equipped with Pt wire work and secondary electrodes, interfaced with a potentiostat/galvanostat VoltaLab PST050 equipment. The cyclic voltammograms were obtained from NBu_4BF_4 solutions in DMF (0.10 M) used as electrolyte. The potentials were measured in Volts (±10 mV) *versus* SCE at 200 mV/s using $[Fe(\eta^5\text{-}C_5H_5)_2]^{0/+}$ (E = 0.47 V; DMF) as the internal reference. The window of potential was established using a solution of the freshly prepared electrolyte.

Transmission Electron Microscopy (TEM): A Hitachi H-8100 electron microscope operated at 200 kV was used to obtain TEM images. A drop of sample solution was deposited and air-dried in a carbon/Formvar-coated copper grid.

3. Results and discussion

3.1. Characterization of GO and $P(NH_2)_{2,adj}$ hybrids

GO was prepared through a variation of Hummers' method and was previously characterized [13] using different spectroscopic techniques all of which confirmed the presence of sp^3 carbon atoms of defects created in the material by the attachment of hydroxyl, carbonyls, carboxylic acid, and epoxy groups. GO samples were subsequently used to interact with the previously synthesized porphyrin, $P(NH_2)_{2,adj}$, through covalent and noncovalent interactions.

TEM studies. The morphology of such GO samples was assessed from microscopic information. TEM images of GO and GO modified covalently and noncovalently with $P(NH_2)_{2,adj}$, are depicted, respectively in Fig. S1 (Supplementary material) and Fig. 1. In opposition to the more transparent single-layer evident of GO sample, both modified GO samples (GO-P and GO + P) evidenced thicker flakes with crumpled structures and with lateral dimensions within the range of submicrometer to 1 μm, clearly indicating the presence of few-layer stacks. The latter are an indication of some induced stacking due to π−π interactions promoted by the presence of the porphyrin units. Such an effect that occurs to a similar extent in both hybrids will favor the excited state electron interaction process between the two components.

FTIR studies. The chemical functionalization of GO was followed by FTIR spectroscopy. The DRIFT spectra of the pure reagents, of a physical mixture (GO + $P(NH_2)_{2,adj}$ mass ratio of 1.0:0.4), of activated GO and the covalent reaction product, GO-$P(NH_2)_{2,adj}$, are presented in Fig. 2. The spectra of the pure $P(NH_2)_{2,adj}$, and GO (a and b, respectively) correlate well with those reported for similar molecules. The proposed band assignments are summarized in Table S1, SI.

In case no reaction occurred between the two components, the spectrum of the so-called reaction product would be similar to that of a physical mixture in the reaction proportions. Comparing spectra 2c (physical mixture) and 2e (covalent reaction product), the first one corresponds to the superposition of those pure molecules, keeping all the observed bands of porphyrin and GO, without band shifts, whereas the latter has obvious differences. These could in principle be explained by the activated GO in the reaction conditions, but a comparison of spectra 2d and 2e shows that this is not the case.

For activated GO, 2d, there is no indication for benzoyl chloride formation [36]. This can be due to the known instability of the acyl chloride terminals that easily hydrolyze restoring the carboxylic acid group. Nevertheless, the band at 1286 cm^{-1} (assigned to ν_{as}COC, epoxy + δCOH mode) is shifted when compared to the pure GO spectrum (at 1226 cm^{-1}) and the same is true for the νCO(H) observed at 1034 cm^{-1} (instead of 1051 cm^{-1} for pure GO). These shifts may be interpreted in terms of different intermolecular interactions upon activation, due to conformational changes that may occur at equilibrium.

The spectrum of the reaction product GO-$P(NH_2)_{2,adj}$, 2e, has a very different pattern when compared to those of pure molecules, physical mixture, or activated GO. In the high-frequency region (3700-2500

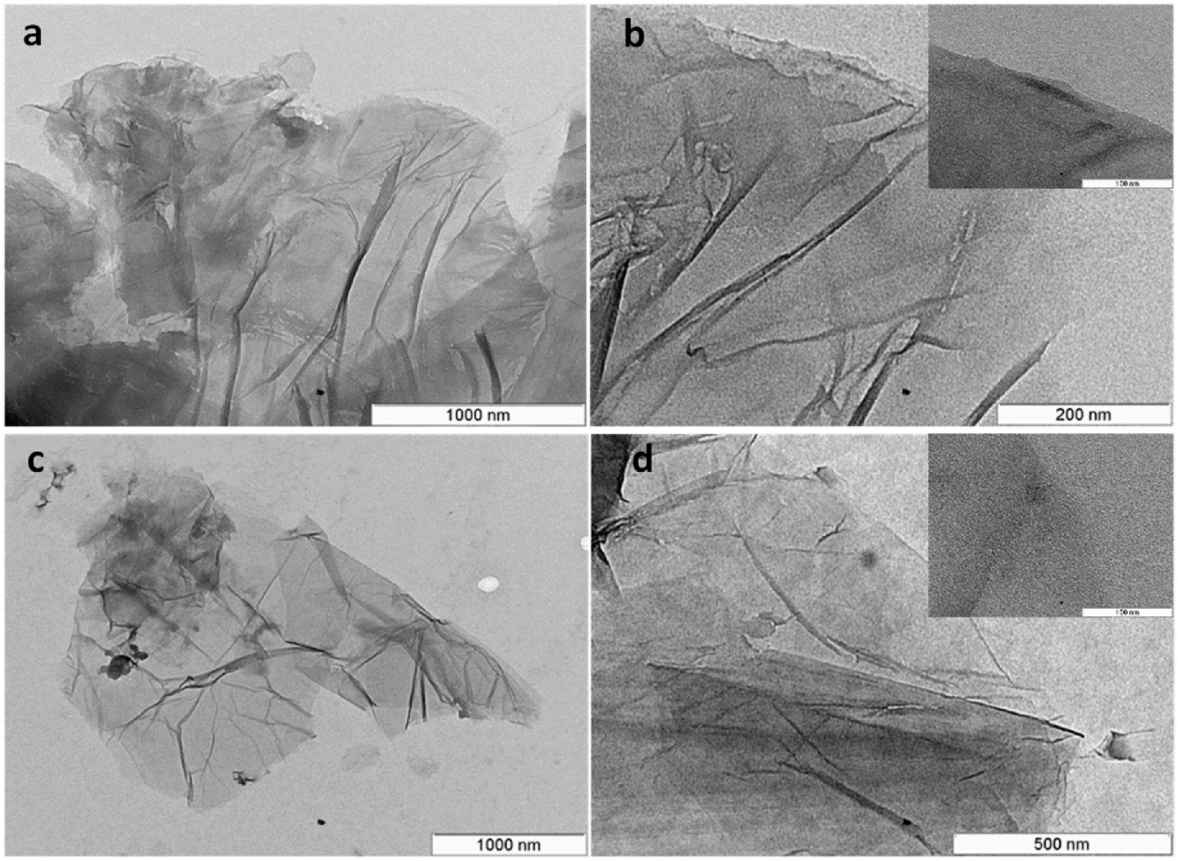

Fig. 1. TEM images of (a–b) synthesized GO-P$(NH_2)_{2,adj}$ covalent; and of (c–d) GO + P$(NH_2)_{2,adj}$ noncovalent hybrids.

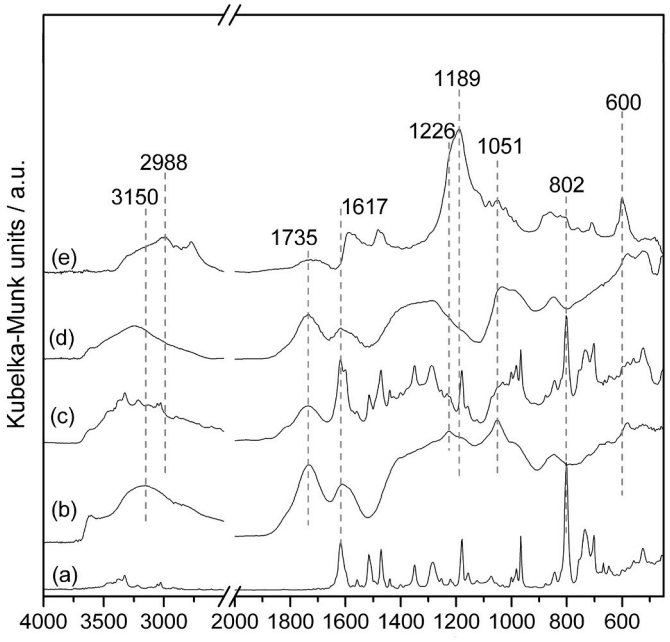

Fig. 2. DRIFT spectra of: (a) pure P$(NH_2)_{2,adj}$; (b) pure GO; (c) GO + P$(NH_2)_{2,adj}$ physical mixture; (d) activated GO; (e) covalent reaction product GO - P$(NH_2)_{2,adj}$.

cm^{-1}) the very broad band appears shifted to lower wavenumbers and has a lower intensity (relative to the maximum) when compared to pure GO or activated GO. Moreover, the porphyrin amine bands are not clear and the shoulder at 3286 cm^{-1} is more correctly assigned to a νNH mode of an amide [37]. In the carbonyl stretching region, the GO band at 1735 cm^{-1} (νC=O) highly decreases and is shifted to lower wavenumber (1729 cm^{-1}), with a shoulder at 1664 cm^{-1}, showing that almost all the acid groups in GO were affected. In fact, the shoulder can be assigned to the νC=O mode of an amide (amide I) [38,39]. Besides, the medium/-strong porphyrin band at 1617 cm^{-1}, assigned to $\delta_{sc}NH_2$, νC··C modes, appears, in the reaction product, at 1587 cm^{-1}, and can also be related to an amide mode, the δCNH (or amide II).

In spectrum 2a, the two bands at 1441 and 1471 cm^{-1} are associated with the porphyrin macrocycle in tetraphenyl porphyrins. The second band is much stronger, as observed for tetra aminophenyl porphyrin. In the GO-P$(NH_2)_{2,adj}$ product, this band is split into two equivalent components (1470/1481 cm^{-1}), which are indicative of redistribution of electronic density in conjugated bonds of porphyrin, consistent with modifications at some of the phenyl substituents. Therefore, there is little evidence of NH_2 groups in the spectrum of the reaction product.

Additional confirmation of the covalent bonding between GO and P$(NH_2)_{2,adj}$ is the band at 600 cm^{-1} that appears only in spectrum 2e and is thus characteristic of the reaction product. It may be assigned to an amide mode (δO=C–N, or τO=C–N–C) [37]. On the other hand, since only a few GO acid groups remain, it is possible to propose that each GO molecule is bound to several porphyrin molecules.

Photoluminescence studies. Due to the complementary electronic properties of carbon materials and porphyrins, both ground state and excited-state electron interactions are expected to reflect both hybrid architectures, either by direct covalent association or by π-π interactions. The potential bioapplications that motivated the present study prompted us to work in an aqueous environment. Due to the poor solubility of the porphyrin and of the hybrid in water an aqueous mixture DW:DMF (2:1 v/v) was used.

The absorption and fluorescence spectra of the hybrids dispersed in solution (DW/DMF 2:1 v/v), are presented in Fig. 3, and are compared

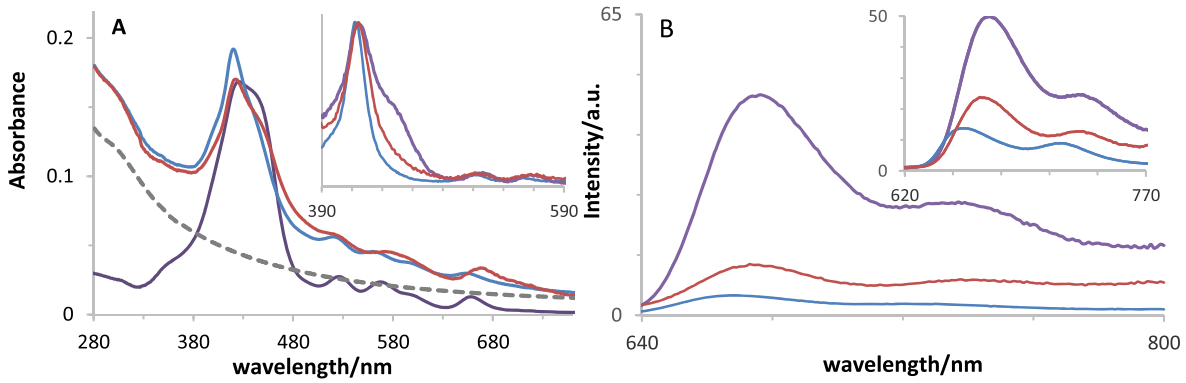

Fig. 3. –Absorption (A), fluorescence (B) and excitation spectra (inset A) of GO (dotted grey), $P(NH_2)_{2,adj}$ (purple), $P(NH_2)_{2,adj}$ - (GO (blue) and $P(NH_2)_{2,adj}$ + GO (red) dispersed in DW/DMF (2:1 v/v). *Inset A*: λ_{emi} = 720 nm; B: λ_{exc} = 455 nm (*inset B*: λ_{exc} = 405 nm).

to those of the porphyrin alone (GO absorption is stronger below 400 nm, although it extends throughout the entire UV–Vis range studied). A preliminary study over time of preparation showed that aging effects are minimal (data not shown), an important aspect in terms of graphene processability.

The absorption spectrum of the porphyrin alone in this solvent mixture denotes considerable changes when compared to that in pure DMF (Fig. S2): the sharp high-energy Soret band at 425 nm in pure solvent appears red-shifted and broader in DW:DMF mixture. This broadening effect is more evident as the amount of water in the mixture increases (fwhm~3670 cm^{-1} in 99% of distilled water (Fig. S2). The decomposition of the Soret band using a sum of Gaussian functions points to the existence of two main contributions with peaks at 425 nm and 450 nm (Fig. S2). According to exciton theory, this red-shifted band is consistent with a head-to-tail arrangement of the monomeric units in an aggregated species stabilized by H-bonding with the aqueous solvent [40–42]. Further insight regarding these aggregates can be obtained from resonance light scattering (RLS) [43]. The intensity of the RLS signal depends on the aggregate size and geometry, the monomer oscillator strength, and the extent of electronic coupling between adjacent chromophores [44]. The RLS signal of P-$(NH_2)_{2,adj}$ in DMF is not significant and shows a trough in the Soret band region corresponding to the loss of photons due to absorption, whereas, in DW:DMF (2:1) a relatively intense resonant peak is observed around 460 nm, Fig. S3. The strong signal is indicative of a large number of interacting chromophore units composing the aggregate or/and strong electronic coupling between transition dipole moments of the porphyrin units.

Nonetheless, due to the electron-donating character of the amino-substituents in *para* positions, red shifts of these bands, as compared to TPP, are expected and can be correlated using Hammett substituent constants which account for resonance and inductive effects [45].

The porphyrin absorption spectra in the hybrids, Fig. 3A, depict distinct features pointing out the electronic perturbation promoted by the interaction with GO. In particular, the Soret band has a peak better defined at 420 nm (monomer) and a less prominent band at 450 nm (aggregate), such differences being more distinct for the covalent hybrid (GO-$P(NH_2)_{2,adj}$). This can be an indirect indication that in the case of the latter the porphyrin must be essentially attached to the GO. The fact that some porphyrin aggregates are still present in the covalent hybrid led us to assume that H-bonding (and π−π interactions) can be established between porphyrins linked to adjacent GO sheets. In the inset of Fig. 3A are shown the excitation spectra obtained at each emission peak (see below) of the hybrids and the porphyrin alone. Whereas in the case of the covalent hybrid, the spectra are almost identical, in the case of GO + $P(NH_2)_{2,adj}$ and $P(NH_2)_{2,adj}$, there is a clear dependence on the emission wavelength and the spectra are distinct from that of absorption, thus implying the co-existence of weakly fluorescent aggregates, most probably J-type aggregates [43,46].

Photoluminescence studies can provide further insight into the electronic interaction between the excited state of porphyrin and GO. The emission spectra of the covalent and noncovalent hybrids in the aqueous mixture DW:DMF (2:1, v/v) were obtained upon excitation at 405 nm and 455 nm (aggregate absorption peak), and compared to those of the porphyrin alone at matching absorbances (OD~0.1), Fig. 3B. Once again, it is possible to detect differences in the position and intensity of the two vibronic bands in the 600 to 800 emission region of the porphyrin upon interaction with GO: a blue-shift, respectively, 6 nm for the noncovalent and 16 nm for the covalent hybrid, and less intense bands relative to the spectrum obtained for the porphyrin alone in the same environment. It is worth mentioning that under both excitation conditions, we did not find any contamination from the intrinsic fluorescence of GO (assuming a similar amount of GO in the covalent and noncovalent samples, based on the comparable absorbance signal obtained for both samples in the UV range).

Further insight into the quenching process, was attempted by widening [GO] and following the effect on the absorption and emission spectra of the porphyrin in the noncovalent hybrid (Fig. S4). There is a concomitant decrease of the absorbance on the red side of the Soret band which presents a sharper profile at higher [GO]. At the same time, the fluorescence intensity decreases without alterations of the spectra profile with increasing additions of GO. These changes indicate that, on one hand, porphyrin aggregates contribute less to the absorption and fluorescence signal with the increase of [GO] due to preferential interactions with the latter. On the other hand, such interactions do not seem to produce additional fluorescent species.

Fluorescence quenching is also evidenced in transient measurements, Fig. S5. A multiexponential decay was obtained for the porphyrin in the solvent mixture, Table 1, denoting the system complexity. The long component is similar to that obtained in neat organic solvents such as tetrahydrofuran or chloroform and can be safely assigned to the porphyrin monomer. The intermediate lifetime was also obtained for the porphyrin in DMF, the difference being its diminute contribution to the overall decay in DMF as compared to the solvent mixture. The sub-nanosecond lifetime was not detected in neat organic solvents but has a considerable contribution in the aqueous solvent mixture. Multiexponential decays presenting shorter lifetimes have already been reported for porphyrins in solution and assigned to specific porphyrin-solvent interaction and/or to porphyrin self-association [46,47]. This component is absent in the hybrid, consistent with spectral blue shifts of absorbance and emission and independence of the excitation spectrum on emission wavelength, Fig. 3. By contrast, it can be found in the noncovalent hybrid although with a smaller contribution compared to the porphyrin alone. Interaction with GO also leads to changes in the two long components: in both hybrids, the contribution of the longer lifetime to the overall decay decreases, whereas a significant quenching of the intermediate lifetime takes place leading to the decrease of the

Table 1
Kinetic analysis of the fluorescence decays of $P(NH_2)_{2,adj}$, and hybrids in DW/DMF (2:1 v/v) (see text for further details).

Sample[a]	ϕ_f/%[b]	τ_{f1}/ns[c]	A_1	τ_{f2}/ns	A_2	τ_{f3}/ns	A_3	k_{ET}/s^{-1}[e]	ϕ_{ET}[f]
$P(NH_2)_{2,adj}$	1.30	**6.56**	0.14	**2.03**	0.26	**0.42**	0.60	–	–
$P(NH_2)_{2,adj}$-GO[d]	0.50	**7.05**	0.05	**1.02**	0.95	—	–	8.3×10^8	0.84
$P(NH_2)_{2,adj}$ + GO[d]	0.90	**7.01**	0.07	**1.35**	0.42	**0.35**	0.51	5.9×10^8	0.79

[a] Data obtained in DW:DMF (2:1).
[b] TPP in cyclohexane ($\phi_f = 10.0\%$) used as reference.
[c] Obtained using $I(t) = \sum_{i=1}^{N} A_i e^{(-t/\tau_{fi})}$ to fit the decays.
[d] For a similar absorbance at the excitation wavelength (OD~0.1).
[e] Obtained using Eq. (1).
[f] Obtained using Eq. (2).

average lifetimes, more pronounced in the covalent hybrid implying a stronger interaction with GO.

Similar to steady-state, changes in fluorescence lifetimes of the porphyrin in the noncovalent hybrid upon increasing [GO] were followed denoting a quenching effect, inset Fig. S4B. These effects can be analyzed using the modified Stern-Volmer equation:

$$\varphi_{fo} / \varphi_f = \tau_{fo} / \tau_f \ (1 + K_s[Q]) \quad (1)$$

with $\tau_{fo}/\tau_f = 1 + K_D$ [Q]; ϕ_{fo} and τ_{fo} are, respectively, the fluorescence quantum yield and lifetime of the porphyrin in the absence of GO (Q, quencher), whereas ϕ_f and τ_f correspond to those obtained after each GO addition; K_D and K_S represent, respectively, the dynamic and static constants. The values obtained $K_D = 19.5$ mL mg^{-1} and $K_S = 61.1$ mL mg^{-1} show the important contribution of the static mechanism to the overall quenching process of $P(NH_2)_{2,adj}$ by GO [14]. These values are of the same order of magnitude as those obtained for tetrahydroxyphenyl porphyrin [48], but are much higher (*ca.* 20 times) than those reported for the tetraphenyl porphyrin interaction with GO [49], which highlights the importance of the porphyrin substituent groups in the interaction with the oxygen groups of GO (*i.e.*, hydrogen bonding).

Given the significant decrease of the porphyrin fluorescence lifetime in presence of GO, it is feasible to assume that an electron transfer and/or energy transfer could be involved in the hybrids.

Fluorescence quenching of porphyrins/phthalocyanines interacting with carbon-based nanostructures such as carbon nanotubes [47,50] or graphene [13,51] have been previously reported and are an indication of electronic interactions in the hybrids between the porphyrinoid excited state and GO moieties. Porphyrins have a relatively high LUMO level, and therefore photoexcited porphyrins are often used as electron donors [52]. Such interactions leading to fluorescence quenching have been assigned mostly to a photoinduced electron transfer process (PET) from the excited donor (porphyrinoid) to the electron-accepting carbon material [53].

Assuming that electron transfer between the porphyrin and GO is the main process involved in the quenching process, we can estimate the rate constant, k_{ET}, and the quantum yield of the process, ϕ_{ET}, Eqs (2) and (3), respectively:

$$k_{ET}(s^{-1}) = (1/\tau_q) - (1/\tau_f) \quad (2)$$

$$\varphi_{ET} = [(1/\tau_q) - (1/\tau_f)] / (1/\tau_q) \quad (3)$$

where, τ_q and τ_f represent the intermediate lifetime of the hybrids and the free porphyrin, respectively. The estimated rate constants, Table 1, point to a more effective process in the covalent hybrid than in the noncovalent one. The value of 8.3×10^8 s^{-1} is within the same order of magnitude as that reported for another covalent hybrid involving the mono-aminophenyl porphyrin derivative in DMF (1.14×10^9 s^{-1} [21]). However, the process was shown to be more efficient in the noncovalent interaction of the cationic porphyrin TMPyP and GO than in our case, probably due to the important electrostatic interactions for the former [22].

The hypothesis of electron transfer as the driving force for fluorescence quenching can be probed in terms of the process thermodynamics, using the Rehm-Weller expression to estimate the free energy change for electron transfer from the singlet excited state of the porphyrin to GO [54]. Using the oxidation potential of the donor Fig. S6 ($E^0_{oxi}(P^{\bullet+}/P)$ =0.78 V *vs.* SCE), obtained from cyclic voltammetry measurements (this value is only *ca.* 100 mV cathodically shifted for the porphyrin in the GO hybrid, 0.68 V [21]), the reported value of −0.79 V for the conduction band edge of GO and independent of the oxidation level [55] (and taking the 0-0 transition of the singlet excited state of $P(NH_2)_{2,adj}$, $\Delta E_{0\text{-}0} = 1.85$ eV (determined from the wavelength at the intersection of the normalized spectra of absorption and emission), the calculated value of the free energy change for this ET process is −0.28 eV. The value is even more negative in the case of the covalent hybrid, −0.98 eV. Negative values are an indication that PET is thermodynamically favorable in both cases.

Further photoluminescence studies may be sought with AuNP which can be added to the GO-P covalent and noncovalent hybrids.

3.2. *Characterization of AuNP@GO-P$(NH_2)_{2,adj}$ hybrids*

AuNP@GO hybrids can be obtained either through *in situ* growth or *ex situ* both of which exhibit long-term stability together with a homogeneous coverage of the graphene sheets [13]. In the present study, we chose the *ex situ* production of AuNP and subsequent addition to the covalent and noncovalent hybrids, to use the same experimental conditions. TEM images (Figure S7A), of AuNPs prepared by the chemical reduction of the metal salt induced by sodium citrate, show essentially spherical AuNP (above 80%) with no apparent tendency to aggregate (confirmed by the corresponding extinction spectrum in an aqueous dispersion with a maximum at *ca.* 523 nm associated to the surface plasmon resonance (SPR) band and absence of any signal at longer wavelengths characteristic of aggregated or rod-like entities) [56]. The sizes obtained are similar to those previously reported using citrate reducing/capping agent [57]: from 15 to 22 nm (with a narrow distribution, average size ~17 nm, Fig. S7B) but, are slightly bigger than the 10 nm average sizes obtained using *in-situ* growth of AuNP through sonolytic reduction [13,58].

AuNPs are expected to interact with GO sheets and to locate preferentially in the basal plane of those sheets. Corresponding TEM images confirm this to be the case of AuNP@GO + $P(NH_2)_{2,adj}$ noncovalent hybrids, Fig. 4B. Besides, in both hybrids, the preferential interaction of AuNP is with GO (almost no AuNP are found outside), Fig. 4. Curiously, there seems to be a preferential location for the NPs on the edges of the GO-$P(NH_2)_{2,adj}$ covalent hybrid, Fig. 4A. These sites correspond essentially to the covalent association of the porphyrin molecules to the GO sheets and point to alterations in the oxygen groups of the basal plane of GO sheets.

Photoluminescence studies were also carried out for these hybrids in DW:DMF (2:1 v/v), and their absorption, fluorescence emission, and excitation spectra were compared to the systems without AuNP, Fig. 5.

No significant changes in the porphyrin absorption spectra were detected apart from those in the Q-band region. These correspond to the

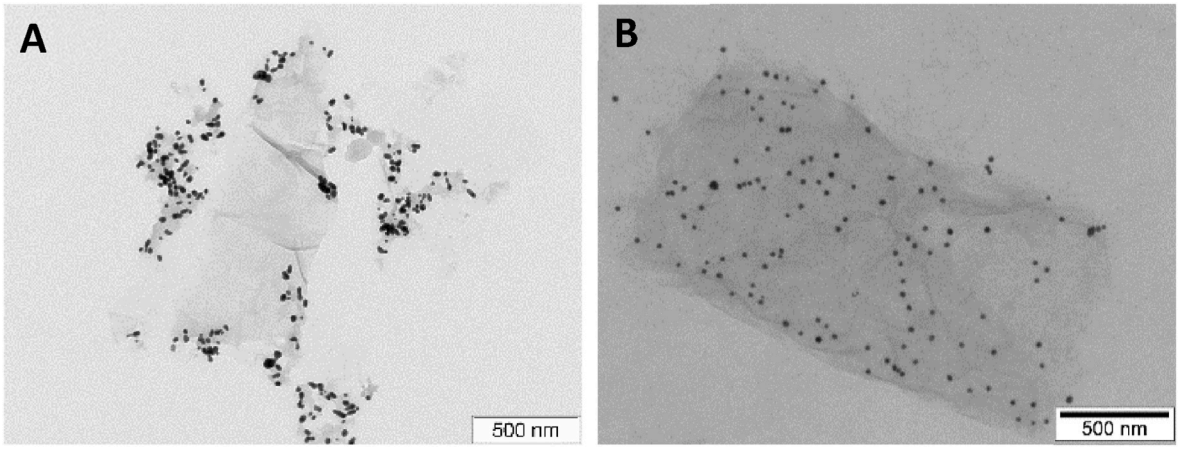

Fig. 4. TEM images of AuNPs adsorbed to (a) covalent GO-$P(NH_2)_{2,adj}$, and to (b) noncovalent GO + $P(NH_2)_{2,adj}$ hybrids.

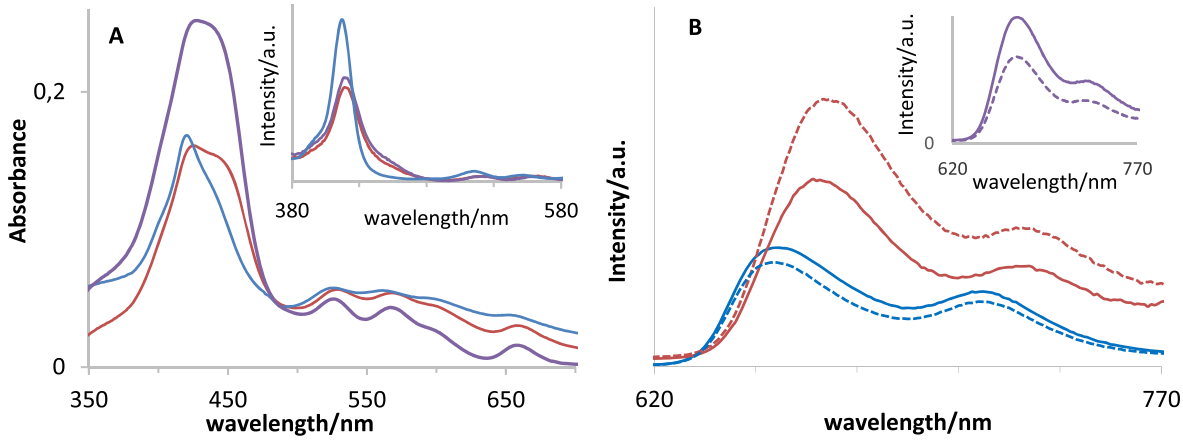

Fig. 5. Effect of the presence of preformed AuNP in A) absorption and B) fluorescence emission spectra (dotted lines) of $P(NH_2)_{2,adj}$ (purple line) interacting covalently (blue line) and noncovalently (red line) with GO dispersed in DW:DMF (2:1 v/v); λ_{exc} = 405 nm. Inset A) excitation spectra, λ_{em} = 650 nm.

contribution of the surface plasmon resonance band of AuNP. The extinction spectrum of AuNP alone in DW-DMF (2:1) mixture (Fig. S8) differs from that obtained in pure water denoting a broadening of the SPR band to the red which points to an increase in polydispersion due to some contribution of nanoparticle aggregation promoted by the lower solvent mixture dielectric constant, as compared to water [59]. NP aggregation tendency decreases in presence of GO sheets which can prevent AuNP agglomeration due to its high dielectric environment [60].

The addition of AuNP seems to affect differently the emission of the porphyrin depending on whether it is covalently or noncovalently associated to GO, Fig. 5B. Under analogous excitation conditions (regardless of the excitation wavelength used, i.e., 405 or 455 nm), there is a quenching effect of the porphyrin fluorescence when covalently associated to GO, which is even more efficient for the porphyrin alone. The lower estimated fluorescence quantum yields of 0.90% for the latter and 0.45% for the porphyrin in the covalent hybrid, represent a quenching of ca. 10% in this case, and 31%, for the porphyrin in the presence of AuNP, Table 2. In turn, an enhancement of more than 30% is detected in the case of the noncovalent association.

The fluorescence decay of the porphyrin after the addition of AuNP remains triexponential, with the shortening of both the long and intermediate lifetimes, Table 2, Fig. S9. A decrease in the average lifetime of the porphyrin occurs for both hybrids as well, although more impactfully in the case of the noncovalent. Still, these results indicate a less significant quenching as compared to those observed above for the fluorescence quantum yields. The values obtained for the radiative (k_r) and nonradiative (k_{nr}) rate constants for the porphyrin in the three systems in presence of AuNP are displayed in Table 2. In brackets, the

Table 2
Kinetic analysis of the fluorescence decays of $P(NH_2)_{2,adj}$, and hybrids upon addition of preformed AuNP in DW/DMF (2:1 v/v).

Sample	ϕ_f/%	τ_{f1}/ns	A_1	τ_{f2}/ns	A_2	τ_{f3}/ns	A_3	$<\tau_f>$/ns[a]	$k_r x10^{-6}$[b,d] /s^{-1}	$k_{nr} x10^{-8}$[c,d] /s^{-1}
$P(NH_2)_{2,adj}$	0.90	**6.49**	0.10	**1.12**	0.25	**0.45**	0.63	1.22	7.4 (7.7)[d]	8.1 (5.8)
$P(NH_2)_{2,adj}$-GO	0.45	**7.01**	0.05	**1.01**	0.95	—	–	1.31	3.4 (3.7)	7.6 (7.5)
$P(NH_2)_{2,adj}$ + GO	0.12	**6.34**	0.05	**1.00**	0.20	**0.56**	0.75	0.94	12.8 (6.6)	10.6 (7.2)

[a] Average lifetime calculated as $<\tau_f> = \sum A_i \times \tau_i$.
[b] $k_r = \phi_f/<\tau>$.
[c] $k_{nr}=(1-\phi_f)/<\tau>$.
[d] Values in brackets were obtained in the absence of AuNP.

values for the rate constants in the absence of AuNP are provided for easier comparison. The presence of AuNP leads to an increase in the nonradiative rate constant in the three systems.

The orientation of the fluorophore dipole moment relative to the metallic surface, and the size and shape of the metal nanostructures, are among the conditions that affect the optical properties of the fluorophores interacting with metallic surfaces. For short distances (usually below 5 nm) [61] additional nonradiative channels (e.g.: via energy transfer, EnT) are promoted by the metal which quenches the fluorophore's emission. The important overlap of the SPR band of the synthesized AuNP with the porphyrin emission, as it is the case, indicates that the energy transfer process may be involved [62]. The constant rate for this extra nonradiative process is $k_{EnT} = 2.3 \times 10^8\ s^{-1}$ for the porphyrin but is one order of magnitude lower in the case of the covalent hybrid. The efficiency of the EnT process can be calculated, $E = 1\text{-}\phi_{D\text{-}A}/\phi_D$ (or $E = 1\text{-}\tau_{D\text{-}A}/\tau_D$) using the fluorescence intensity of the porphyrin (or P(NH$_2$)$_{2,adj}$-GO) in presence of AuNP and its absence, respectively, Table 2. The highest efficiency for EnT was obtained for the porphyrin alone, 31%. Due to the very low fluorescence quantum yield of the porphyrin in the covalent hybrid, the efficiency for ET is expected to be lower, as is the case, ca. 10%.

This EnT process is traditionally described by Förster theory, where the dipole of the porphyrin can efficiently couple to the dipole of the SPR field near the gold nanoparticle. FRET efficiency, E_{FRET}, is inversely proportional to the sixth power of the distance between donor-acceptor FRET pair, r, and occurs within 2–8 nm distance:

$$E_{FRET} = \frac{1}{1 + \left(\frac{r}{R_0}\right)^6} \tag{4}$$

where R_0 is the critical distance at which energy transfer and spontaneous decay are equally probable and can be obtained by:

$$R_0 = 0.2108 \left[k^2 \varphi_D n^{-4} \int_0^\infty I_D(\lambda) \varepsilon_A(\lambda) \lambda^4 d\lambda \right]^{1/6} \Big/ \mathring{A} \tag{5}$$

where k^2 is the orientation factor, ϕ_D is the donor fluorescence quantum yield, n is the refractive index of the medium, and the integral accounts for the overlap between the fluorescence spectrum of the donor and the molar absorption coefficient of the acceptor. The calculated R_0 11.5 nm was used to obtain the distance between donor and acceptor, r, 13.2 nm. This value is above the upper limit of the FRET useful efficiency. There have been several studies in the literature involving organic/inorganic donors-gold nanoparticle acceptor pairs with similar distance-dependent energy transfer results [63]. Sen & Patra reported a Förster distance of 103.56 Å for the resonance energy transfer from R6G to 3-nm spherical AuNP [64]. A study involving photoluminescence lifetime quenching of terbium complexes (Tb) conjugated to streptavidin (sAv) and bound to biotinylated AuNPs of different diameters (5, 30, 50, and 80 nm) also confirms that the assumption of a point dipole for both donor and acceptor, as in FRET model, does not adequately describe the strongly coupled limit for dipoles in AuNP [65].

Nanosurface energy transfer (NSET) has emerged as an energy-transfer mechanism that, in contrast to FRET, considers the acceptor as a nanometric surface modeled as a collection of many dipoles. In this model, efficiency is inversely proportional to the fourth power of the separation distance between donor and acceptor:

$$E_{NSET} = \frac{1}{1 + \left(\frac{d}{d_0}\right)^4} \tag{6}$$

Similar to R_0, d_0 is the distance at which a dye will display equal probabilities for energy transfer and spontaneous emission, and can be calculated by using Persson model [66].

$$d_0 = \left(\frac{0.225 c^3 \varphi_D}{\omega_D^2 \omega_F k_F} \right)^{1/4} \tag{7}$$

where c is the speed of light, ω_D is the angular frequency resonant with the donor electronic transition ($\omega_D = 2\pi c\lambda^{-1}$), ω_F and k_F are, respectively, the angular frequency and the Fermi vector for bulk gold ($\omega_F = 8.4 \times 10^{15}\ s^{-1}$ and $k_F = 1.2 \times 10^{10}\ m^{-1}$). The d_0 value obtained of 3.2 nm was used to retrieve the donor-acceptor distances, d, of 4.0 nm, below 5 nm [61]. Similar values of donor−acceptor distances within the range of 4.0–6.4 nm were afforded by using the NSET model, consistent with the expected structure of Tb-streptavidin/biotin-AuNP assemblies [65]. Interestingly, these values were independent of the AuNP diameter (5–80 nm).

As mentioned above, the electromagnetic field of metal NPs can either quench or enhance the fluorescence of nearby fluorophores. The latter seems to be the dominant process in the case of the interaction of the porphyrin + GO noncovalent hybrid with the AuNP. While a decrease of the radiative rate constant (less than 10%) occurs for the porphyrin and covalent hybrid the reverse is observed for the noncovalent hybrid in presence of AuNP.

An enhancement of the fluorescence through the increase of excitation rates and radiative rates is effective up to longer distances from the metal nanoparticle's surface [61]. For fluorophore-metal separation distances above 5 nm up to 10 nm, the fluorescence enhancement effect reaches its maximum [67]. MEF has been related to both the increased excitation rate due to the enhancement of the local electrical field experienced by the fluorophore and the electromagnetic coupling of the dye with the metal nanoparticle, allowing the metal to partially transfer the excitation energy non-radiatively to the dyes.

In the present situation, AuNP interacts with the porphyrin alone at distances short enough to promote nonradiative deactivation of the porphyrin excited states. This seems to be also the case for the covalent hybrid, where AuNP locate preferentially near the GO edges (i.e., near porphyrin units), considering TEM images (Fig. 4A). By contrast, in the noncovalent hybrid, AuNP locates preferentially in the basal plane of the GO sheets stabilized by interactions with the oxygen groups and amino groups of the porphyrin. Therefore, in the noncovalent hybrid, there can be distinct AuNP–P(NH$_2$)$_{2,adj}$ distances, which on average, are those suitable for MEF to take place.

3.3. FLIM images of deposited samples of the hybrids

FLIM was used to gain further insight into the electronic communication between porphyrin and GO [13,34,35,47,68]. Since MEF affects both radiative and nonradiative decay rates, further information regarding the excited states interaction of P(NH$_2$)$_{2,adj}$ with AuNP@GO can be retrieved from emission decay profile analysis. Furthermore, images can be spatially resolved based on the fluorophore lifetime which reports on the fluorophore microenvironment conditions independently of concentration, thus, providing further information about AuNP distribution and interactions with P(NH$_2$)$_{2,adj}$/GO hybrids.

A preliminary test of the possible background interference from GO and AuNP on the porphyrin fluorescence signal was made to set the suitable conditions to have the "cleanest" signal from the porphyrin. Samples morphology attained confirms our solution data: films obtained from DMF (or ACNT) solutions, lead to uniform images for the porphyrin alone whereas a heterogeneous image is obtained for the porphyrin in the aqueous mixture DW:DMF with shorter lifetimes in agreement with porphyrin self-aggregation, Fig. S10.

In the next step, films containing GO and P(NH$_2$)$_{2,adj}$ covalent and noncovalent hybrids were observed, Fig. 6, upper row. In close agreement with TEM, FLIM images show the existence of GO "flakes" with sizes up to a few micrometers. Data obtained show that both covalent and noncovalent interactions between porphyrin and GO lead to a strong quenching of the porphyrin fluorescence, also reflected in shorter

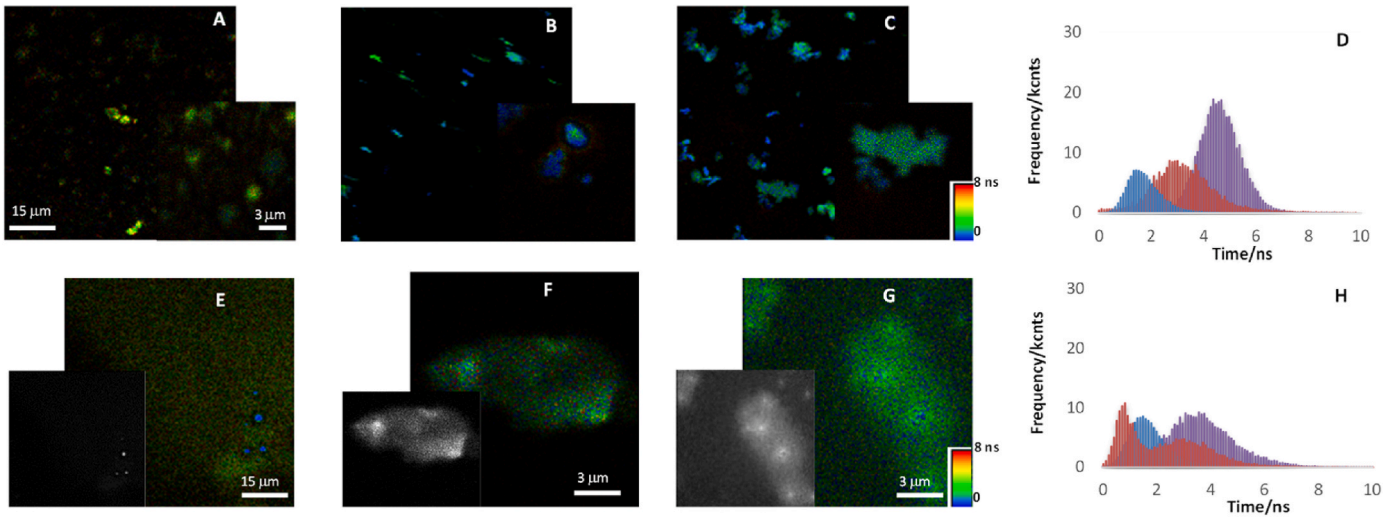

Fig. 6. *Upper row*: FLIM images (A,B,C), with zooms of deposited samples of (A) free $P(NH_2)_{2,adj}$; (B) covalently associated to GO ($P(NH_2)_{2,adj}$ – GO); and (C) noncovalently associated to GO ($P(NH_2)_{2,adj}$ + GO). (D) Fluorescence lifetime distribution obtained from decay analysis of *ca.* 20 point measurements of $P(NH_2)_{2,adj}$ (purple); $P(NH_2)_{2,adj}$ – GO (blue) and $P(NH_2)_{2,adj}$ + GO (red). $\lambda_{exc} = 638$ nm. *Lower row*: FLIM images (E,F,G) and insets showing the respective intensity images of deposited DW:DMF (2:1 v/v) dispersions of preformed AuNP interacting with (E) free $P(NH_2)_{2,adj}$; (F) covalent hybrid, $P(NH_2)_{2,adj}$ – GO; and (G) noncovalently associated to GO $P(NH_2)_{2,adj}$ + GO. (H) Fluorescence lifetime distribution (colours have the same meaning as in (D)). $\lambda_{exc} = 638$ nm.

fluorescence lifetimes, Fig. 6C. As in solution, the process seems to be more efficient in the case of the covalent association given the porphyrin average fluorescence lifetime of ≈1.7 ns obtained for the latter, in clear contrast with that of the free porphyrin ($\tau_{avg} \sim 5$ ns). Data support an efficient fluorescence quenching of the porphyrin excited-states upon interaction with GO especially when a covalent bond is involved. Similar reports involving the rapid deactivation of porphyrin excited-state upon interaction with carbon nanomaterials were assigned to intracomplex charge separation [69].

The effect of the addition of pre-formed AuNPs on the porphyrin fluorescence was also followed for both hybrids through FLIM. It is possible to detect short-lived bright round-shaped entities essentially localized on the surface of GO flakes, Fig. 6, lower row. AuNPs were also added to the porphyrin alone in the solvent mixture, which seems to have a de-aggregated effect on the porphyrin, considering the more homogeneous image obtained, Fig. 6E. Nonetheless, the broad histogram associated with this image is shifted to shorter lifetimes, Fig. 6H, and has fewer counts, when compared to that of the porphyrin alone. This is a clear indication of quenching within the porphyrin fluorescence promoted by its interaction with AuNPs. The histograms show relatively broad lifetime distributions especially in the case of the porphyrin and the noncovalent hybrid, reflecting the heterogeneity of these films. A low frequency of lifetimes in the range of 6–8 ns was obtained for these systems which can be assigned to the existence of a residual contribution from non-associated porphyrin (monomers) existing after solvent evaporation.

A distinct pattern can be found for the porphyrin associated to GO, in which case the addition of AuNPs can be visualized by bright spots almost exclusively on the surface of GO flakes, Fig. 6F and G. This leads to a histogram for the porphyrin very similar to that obtained without AuNPs, in the case of the covalent hybrid, Fig. 6H. However, the histogram changes considerably in the case of the noncovalent association denoting an extended contribution of fluorescence lifetimes. The existence of bright spots is associated with shorter lifetimes [70]. These differences can be accounted by the effect of AuNPs' metallic surface on the porphyrin radiative and nonradiative decay rates, as seen above in solution. As shown above, for distances below 5 nm MEF may not be effective due to nonradiative energy. For distances longer than 20 nm the weak electromagnetic field prevents its efficiency. Since AuNPs tend to locate on the GO surface, the probability of having porphyrins at adequate distances is higher in the case of the noncovalent hybrid justifying the histogram extension toward short lifetimes. The fact that there is no clear MEF evidence in the case of the covalent hybrid leads us to assume that the interaction GO - AuNP is rather important.

4. Conclusions

In this contribution, we have demonstrated the electronic communication of oxidized graphene with an amino derivatized porphyrin present either covalently attached or interacting noncovalently with GO sheets. From the DRIFT spectra analysis, it is possible to conclude that a covalent bond was formed involving the GO acid group and $P(NH_2)_{2,adj}$ amine group, leading to the formation of amide groups. Given that there is no clear indication of the presence of NH_2 in the product, most porphyrin molecules were probably bound to two GO sheets. Both hybrids could be well dispersed in the aqueous mixture (DW:DMF) and the UV–Vis absorption spectra confirmed the preferential porphyrin-GO interactions, which in the case of the noncovalent hybrid is of H-bonding and π−π nature. By contrast, for each element alone in the same medium, porphyrin-porphyrin and GO-GO interactions prevail. Although the quenching of the porphyrin fluorescence can be detected for both systems, the process is more efficient in the case of the covalent hybrid. A faster decay is obtained for the latter, which may be an indication that this type of interaction is more efficient than π−π or H-bond association in electronic communication. The distinct type of GO-porphyrin association also leads to a different electronic response in the presence of pre-formed AuNP. An enhancement of the porphyrin fluorescence is obtained in the case of the noncovalent hybrid by contrast to a quenching effect for the covalent one. A similar behavior takes place in films as evidenced by FLIM. The decrease of the fluorescence lifetime combined with an increased intensity is a signal for an adequate average distance between the metal surface of the AuNP and the porphyrin moieties, whereas, in the hybrid little interaction is detected. We believe these results showed the potential interest of the noncovalent hybrids Au@GO + P in the fields of imaging and biosensing. In turn, GO electron acceptor ability revealed in the covalent GO-P hybrid has a potential interest in the design of novel light-harvesting systems.

Author contributions

The manuscript was written through the contributions of all authors and all have approved the final version of the manuscript.

Declaration of competing interest

The authors declare that they have no known competing financial interests or personal relationships that could have appeared to influence the work reported in this paper.

Data availability

No data was used for the research described in the article.

Acknowledgments

Thanks are due to Fundação para a Ciência e a Tecnologia (FCT, Portugal) for financial support through projects REEQ/115/QUI/2005, Pest-OE/QUI/UI0100/2013/2014, PTDC/QUI-QUI/117498/2010, PTDC/QUI-COL/29379/2017 and, where applicable, co-financing by the FEDER, within the PT2020 Partnership Agreement, as well as to the Portuguese NMR Network. The authors are also grateful to the University of Aveiro and FCT for the financial support of LAVQ-REQUIMTE (UIDB/50006/2020).

Appendix A. Supplementary data

Supplementary data to this article can be found online at https://doi.org/10.1016/j.jlumin.2022.119097.

References

[1] D. Gust, T.A. Moore, A.L. Moore, Mimicking photosynthetic solar energy transduction, Acc. Chem. Res. 34 (2001) 40–48.
[2] G.D. Scholes, G.R. Fleming, A. Olaya-Castro, R. van Grondelle, Lessons from nature about solar light harvesting, Nat. Chem. 3 (2011) 763–774.
[3] S. Mathew, A. Yella, P. Gao, R. Humphry-Baker, B.F.E. Curchod, N. Ashari-Astani, I. Tavernelli, U. Rothlisberger, M.K. Nazeeruddin, M. Graetzel, Dye-sensitized solar cells with 13% efficiency achieved through the molecular engineering of porphyrin sensitizers, Nat. Chem. 6 (2014) 242–247.
[4] V. Strauss, A. Roth, M. Sekita, D.M. Guldi, Efficient energy-conversion materials for the future: understanding and tailoring charge-transfer processes in carbon nanostructures, Chem 1 (2016) 531–556.
[5] G. Bottari, M.Á. Herranz, L. Wibmer, M. Volland, L. Rodríguez-Pérez, D.M. Guldi, A. Hirsch, N. Martín, F. D'Souza, T. Torres, Chemical functionalization and characterization of graphene-based materials, Chem. Soc. Rev. 46 (2017) 4464–4500.
[6] S. Supriya, V.S. Shetti, G. Hegde, Conjugated systems of porphyrin–carbon nanoallotropes: a review, New J. Chem. 42 (2018) 12328–12348.
[7] A.H. Castro Neto, F. Guinea, N.M.R. Peres, K.S. Novoselov, A.K. Geim, The electronic properties of graphene, Rev. Mod. Phys. 81 (2009) 109–162.
[8] H. Hayashi, I.V. Lightcap, M. Tsujimoto, M. Takano, T. Umeyama, P.V. Kamat, H. Imahori, Electron transfer cascade by organic/inorganic ternary composites of porphyrin, zinc oxide nanoparticles, and reduced graphene oxide on a tin oxide electrode that exhibits efficient photocurrent generation, J. Am. Chem. Soc. 113 (2011) 7684–7687.
[9] A.R. Monteiro, C.I.V. Ramos, S. Fateixa, N.M.M. Moura, M.G.P.M.S. Neves, T. Trindade, Hybrids based on graphene oxide and porphyrin as tools for detection and stabilization of DNA G-quadruplexes, ACS Omega 3 (2018) 11184–11191.
[10] A. Lopez, J. Liu, Covalent and noncovalent functionalization of graphene oxide with DNA for smart sensing, Adv. Intell. Syst. 2 (13) (2020), 2000123.
[11] R. Costa-Almeida, D. Bogas, J.R. Fernandes, L. Timochenco, F.A.L.S. Silva, J. Meneses, I.C. Gonçalves, F.D. Magalhães, A.M. Pinto, Near-infrared radiation-based mild photohyperthermia therapy of non-melanoma skin cancer with pegylated reduced nanographene oxide, Polymers 12 (19) (2020) 1840.
[12] I.A. Vacchi, S. Guo, J. Raya, A. Bianco, C. Ménard-Moyon, Strategies for the controlled covalent double functionalization of graphene oxide, Chem. Eur J. 26 (2020) 6591–6598.
[13] S.M. Andrade, C.J. Bueno-Alejo, V.V. Serra, J.M.M. Rodrigues, , M. G. P. M. S. Neves, A.S. Viana, S.M.B. Costa, Anchoring of gold nanoparticles on graphene oxide and noncovalent interactions with porphyrinoids, Chem Nano Mat. 1 (2015) 502–510.
[14] D. Larowska, A. Wojcik, M. Mazurkiewicz-Pawlicka, A. Malolepszy, L. Stobiński, B. Marciniak, A. Lewandowska-Andralojc, Cationic porphyrin-graphene oxide hybrid: donor-acceptor composite for efficient photoinduced electron transfer, ChemPhysChem 20 (2019) 1054–1066.
[15] M. Barrejón, L.M. Arellano, F. D'Souza, F. Langa, Bidirectional charge-transfer behavior in carbon-based hybrid nanomaterials, Nanoscale 11 (2019) 14978–14992.
[16] M. Gosika, V. Velachi, M.N.D.S. Cordeiro, P.K. Maiti, Covalent functionalization of graphene with PAMAM dendrimer and its implications on graphene's dispersion and cytotoxicity, ACS Appl. Polym. Mater. 2 (2020) 3587–3600.
[17] S. Navaljn, J.R. Herance, M. Álvaro, H. Garcia, Covalently modified graphenes in catalysis, electrocatalysis and photoresponsive materials, Chem. Eur J. 23 (2017) 15244–15275.
[18] A. Wang, J. Ye, M.G. Humphrey, C. Zhang, Graphene and carbon-nanotube nanohybrids covalently functionalized by porphyrins and phthalocyanines for optoelectronic properties, Adv. Mater. 30 (2018) 17057041–17057049.
[19] A.R. Monteiro, , M. G. P. M. S. Neves, T. Trindade, Functionalization of graphene oxide with porphyrins: synthetic routes and biological applications, Chem Plus Chem. 85 (2020) 1857–1880.
[20] Y. Xu, Z. Liu, X. Zhang, Y. Wang, J. Tian, Y. Huang, Y. Ma, X. Zhang, Y. Chen, A graphene hybrid material covalently functionalized with porphyrin: synthesis and optical limiting property, Adv. Mater. 21 (2009) 1275–1279.
[21] N. Karousis, A.S.D. Sandanayaka, T. Hasobe, S.P. Economopoulos, E. Sarantopoulou, N. Tagmatarchis, Graphene oxide with covalently linked porphyrin antennae: synthesis, characterization and photophysical properties, J. Mater. Chem. 21 (2011) 109–117.
[22] N. El-Shafai, M.E. El-Khouly, M. El-Kemary, M.S. Ramadana, M.S. Masoud, Self-assembly of porphyrin on graphene oxide in aqueous medium: fabrication, characterization, and photocatalytic studies, Photochem. Photobiol. Sci. 18 (2019) 2071–2079.
[23] I.V. Lightcap, T.H. Kosel, P.V. Kamat, Anchoring semiconductor and metal nanoparticles on a two-dimensional catalyst mat. Storing and shuttling electrons with reduced graphene oxide, Nano Lett. 10 (2010) 577–583.
[24] S. Rodríguez-García, R. Santiago, D. López-Díaz, M.D. Mercán, M.M. Velázquez, J. L.G. Fierro, J. Palomar, Role of the structure of graphene oxide sheets on the CO_2 adsorption properties of nanocomposites based on graphene oxide and polyaniline or Fe_3O_4 –nanoparticles, ACS Sustainable Chem. Eng. 7 (2019) 12464–12473.
[25] Y.-H. Lee, G. Kim, M. Joe, J.-H. Jang, J. Kim, K.-R. Lee, Y.-U. Kwo, Enhancement of electrocatalytic activity of gold nanoparticles by sonochemical treatment, Chem. Commun. (J. Chem. Soc. Sect. D) 46 (2010) 5656–5658.
[26] Y.-Y. Peng, D. Guo, W. Ma, Y.-T. Long, Intrinsic electrocatalytic activity of gold nanoparticles measured by single entity electrochemistry, Chem electro chem. 5 (2018) 2982–2985.
[27] L.A. Austin, M.A. Mackey, E.C. Dreaden, M.A. El Sayed, The optical, photothermal, and facile surface chemical properties of gold and silver nanoparticles in biodiagnostics, therapy, and drug delivery, Arch. Toxicol. 88 (2014) 1391–1417.
[28] V. Amendola, R. Pilot, M. Frasconi, O.M. Maragò, M.A. Iatì, Surface plasmon resonance in gold nanoparticles: a review, J. Phys. Condens. Matter. 29 (2017), 203002.
[29] L.M. Cucci, I. Naletova, G. Consiglio, C. Satriano, A hybrid nanoplatform of graphene oxide/nanogold for plasmonic sensing and cellular applications at the nanobiointerface, Appl. Sci. 9 (2019) 676–689.
[30] C. Joyce, S.M. Fothergill, F. Xie, Recent advances in gold-based metal enhanced fluorescence platforms for diagnosis and imaging in the near-infrared, Mater, Today Adv. 7 (2020), 100073.
[31] J. Tang, L. Niu, J. Liu, Y. Wang, Z. Huang, S. Xie, L. Huang, Q. Xu, Y. Wang, L. A. Belfiore, Effect of photocurrent enhancement in porphyrin-graphene covalent hybrids, Mater. Sci. Eng. C 34 (2014) 186–192.
[32] R. Luguya, L. Jaquinoid, F.R. Fronczek, M.G.H. Vicente, K.M. Smith, Synthesis and reactions of meso-(p-nitrophenyl)porphyrins, Tetrahedron 60 (2004) 2757–2763.
[33] P. Kubelka, F. Munk, Ein Beitrag zur Optik der Farbanstriche, Z. Tech. Phys. 12 (1931) 593–601.
[34] V.V. Serra, S.M. Andrade, , M. G. P. M. S. Neves, J.A.S. Cavaleiro, S.M.B. Costa, J-aggregate formation in bis-(4-carboxyphenyl)porphyrins in water: pH and counterion dependence, New J. Chem. 34 (2010) 2757–2765.
[35] R. Teixeira, V.V. Serra, D. Botequim, P.M.R. Paulo, S.M. Andrade, S.M.B. Costa, Fluorescence spectroscopy of porphyrins and phthalocyanines: some insights into supramolecular self-assembly, microencapsulation and imaging microscopy, Molecules 26 (2021) 4264.
[36] I. Hannus, T. Kollár, Z. Kónya, I. Kiricsi, IR spectroscopic investigations of the adsorption of benzoyl chloride in zeolites, Vib. Spectrosc. 22 (2000) 29–37.
[37] G. Socrates, in: Infrared and Raman Characteristic Group Frequencies, third ed., Wiley&Sons Ltd, UK, 2004.
[38] R. Yamuna, S. Ramakrishnan, K. Dhara, R. Devi, N.K. Kothurkar, E. Kirubha, P. K. Palanisamy, Synthesis, characterization, and nonlinear optical properties of graphene oxide functionalized with tetra-amino porphyrin, J. Nanoparticle Res. 15 (2013) 1399–1408.
[39] Z.-B. Liu, Y.-F. Xu, X.-Y. Zhang, X.-L. Zhang, Y.-S. Chen, J.-G. Tian, Porphyrin and fullerene covalently functionalized graphene hybrid materials with large nonlinear optical properties, J. Phys. Chem. B 113 (2009) 9681–9686.
[40] N.C. Maiti, S. Mazumdar, N. Periasamy, J- and H-aggregates of porphyrin-surfactant complexes: time-resolved fluorescence and other spectroscopic studies, J. Phys. Chem. B 102 (1998) 1528–1538.
[41] S.C. Doan, S. Shanmugham, D.E. Aston, J.L. McHale, Counterion dependent dye aggregates: nanorods and nanorings of tetra(p-carboxyphenyl)porphyrin, J. Am. Chem. Soc. 127 (2005) 5885–5892.

[42] S.M. Andrade, R. Teixeira, S.M.B. Costa, A.J.F.N. Sobral, Self-aggregation of free base porphyrins in aqueous solution and in DMPC vesicles, Biophys. Chem. 133 (2008) 1–10.
[43] S.M. Andrade, S.M.B. Costa, Spectroscopic studies of water-soluble porphyrins with protein encapsulated in bis(2-ethylhexyl)sulfosuccinate (AOT) reverse micelles: aggregation versus complexation, Chem. Eur J. 12 (2006) 1046–1057.
[44] R.F. Pasternack, P.J. Collings, Resonance light scattering – a new technique for studying chromophore aggregation, Science 269 (1995) 935–939.
[45] J.R. Weinkauf, S.W. Cooper, A. Schweiger, C.C. Wamser, Substituent and solvent effects on the hyperporphyrin spectra of diprotonated tetraphenylporphyrins, J. Phys. Chem. A 107 (2003) 3486–3496.
[46] R. Teixeira, S.M. Andrade, V.V. Serra, P.M.R. Paulo, A. Sánchez-Coronilla, , M. G. P. M. S. Neves, J.A.S. Cavaleiro, S.M.B. Costa, Reorganization of self-assembled dipeptide porphyrin J-aggregates in water-ethanol mixtures, J. Phys. Chem. B 116 (2012) 2396–2404.
[47] S.M. Andrade, P. Raja, V.K. Saini, A.S. Viana, P. Serp, S.M.B. Costa, Polyelectrolyte-assisted noncovalent functionalization of carbon nanotubes with ordered self-assemblies of a water-soluble porphyrin, ChemPhysChem 13 (2012) 3622–3631.
[48] R. Ge, X. Wang, C. Zhang, S.-Z. Kang, L. Qin, G. Li, X. Li, The influence of combination mode on the structure and properties of porphyrin-graphene oxide composites, Colloids Surf. A Physicochem. Eng. Asp. 483 (2015) 45–52.
[49] T. Phuangburee, D. Solonenko, N. Plainpan, P. Thamyongkit, D.R.T. Zahn, S. Unarunotai, T. Tuntulani, P. Leeladee, Surface modification of graphene oxide via noncovalent functionalization with porphyrins for selective photocatalytic oxidation of alcohols, New J. Chem. 44 (2020) 8264–8272.
[50] A. Kongkanand, R.M. Dominguez, P.V. Kamat, Single wall carbon nanotube scaffolds for photoelectrochemical solar cells. Capture and transport of photogenerated electrons, Nano Lett. 7 (2007) 676–680.
[51] N. Karousis, J. Ortiz, K. Ohkubo, T. Hasobe, S. Fukuzumi, A. Sastre-Santos, N. Tagmatarchis, Zinc phthalocyanine-graphene hybrid material for energy conversion: synthesis, characterization, photophysics, and photoelectrochemical cell preparation, J. Phys. Chem. C 116 (2012) 20564–20573.
[52] S. Ishihara, J. Labuta, W. Van Rossom, D. Ishikawa, K. Minami, J.P. Hill, K. Ariga, Porphyrin-based sensor nanoarchitectonics in diverse physical detection modes, Phys. Chem. Chem. Phys. 16 (2014) 9713–9746.
[53] A. Wojcik, P.V. Kamat, Reduced graphene oxide and porphyrin: an interactive affair in 2-D, ACS Nano 4 (2010) 6697–6706.
[54] D. Rehm, A. Weller, Kinetics of fluorescence quenching by electron and H-atom transfer, Isr. J. Chem. 8 (1970) 259–271.
[55] T.-F. Yeh, F.-F. Chan, C.-T. Hsieh, H. Teng, Graphite oxide with different oxygenated levels for hydrogen and oxygen production from water under illumination: the band positions of graphite oxide, J. Phys. Chem. C 115 (2011) 22587–22597.
[56] P. Di Pietro, G. Strano, L. Zuccarello, C. Satriano, C. Gold and silver nanoparticles for applications in theranostics, Curr. Top. Med. Chem. 16 (2016) 3069–3102.
[57] G. Gonçalves, P.A.A.P. Marques, C.M. Granadeiro, H.I.S. Nogueira, M.K. Singh, J. Grácio, Surface modification of graphene nanosheets with gold nanoparticles: the role of oxygen moieties at graphene surface on gold nucleation and growth, Chem. Mater. 21 (2009) 4796–4802.
[58] K. Vinodgopal, B. Neppolian, I.V. Lightcap, F. Grieser, M. Ashokkumar, P.V. Kamat, Sonolytic design of graphene−Au nanocomposites. Simultaneous and sequential reduction of graphene oxide and Au(III), J. Phys. Chem. Lett. 1 (2010) 1987–1993.
[59] S.K. Ghosh, T. Pal, Interparticle coupling effects on the surface plasmon resonance of gold nanoparticles: from theory to applications, Chem. Rev. 107 (2007) 4797–4862.
[60] D. Hernández-Sánchez, G. Villabona-Leal, I. Saucedo-Orozco, V. Bracamonte, E. Pérez, C. Bittencourt, M. Quintana, Stable graphene oxide–gold nanoparticle platforms for biosensing applications, Phys. Chem. Chem. Phys. 20 (2018) 1685–1692.
[61] J.R. Lakowicz, K. Ray, M. Chowdhury, H. Szmacinski, Y. Fu, J. Zhang, K. Nowaczyk, Plasmon-controlled fluorescence: a new paradigm in fluorescence spectroscopy, Analyst 133 (2008) 1308–1346.
[62] A. Kotiaho, R. Lahtinen, H. Lehtivuori, N.V. Tkachenko, H. Lemmetyinen, Photoinduced energy and charge transfer in layered porphyrin-gold nanoparticle thin films, J. Phys. Chem. C 112 (2008) 10316–10322.
[63] C. Chen, N. Hildebrandt, Resonance energy transfer to gold nanoparticles: NSET defeats FRET, Trends Anal. Chem. 123 (2020), 115748.
[64] T. Sen, A. Patra, Resonance energy transfer from rhodamine 6G to gold nanoparticles by steady-state and time-resolved spectroscopy, J. Phys. Chem. C 112 (2008) 3216–3222.
[65] C. Chen, C. Midelet, S. Bhuckory, N. Hildebrandt, M.H.V. Werts, Nanosurface energy transfer from long-lifetime terbium donors to gold nanoparticles, J. Phys. Chem. C 122 (30) (2018), 17566e17574.
[66] C.S. Yun, A. Javier, T. Jennings, M. Fisher, S. Hira, S. Peterson, B. Hopkins, N. O. Reich, G.F. Strouse, Nanometal surface energy transfer in optical rulers, breaking the FRET barrier, J. Am. Chem. Soc. 127 (2005) 3115–3119.
[67] N.S. Abadeer, M.R. Brennan, W.L. Wilson, C.J. Murphy, Distance and plasmon wavelength dependent fluorescence of molecules bound to silica-coated gold nanorods, ACS Nano 26 (2014) 8392–8406.
[68] B.Y. Mao, D.G. Calatayud, V. Mirabello, N. Kuganathan, H.B. Ge, R.M.J. Jacobs, A. M. Shepherd, J.A.R. Martins, J.B. De la Serna, B.J. Hodges, S.W. Botchway, S. I. Pascu, Fluorescence-lifetime imaging and super-resolution microscopies shed light on the directed- and self-assembly of functional porphyrins onto carbon nanotubes and flat surfaces, Chem. Eur J. 23 (2017) 9772–9789.
[69] D. Baskaran, J.W. Mays, X.P. Zhang, M.S. Bratcher, Carbon nanotubes with covalently linked porphyrin antennae: photoinduced electron transfer, J. Am. Chem. Soc. 127 (2005) 6916–6917.
[70] V. Vaz Serra, S.G. Serra, M.C.S. Vallejo, P.M.R. Paulo, N.M.M. Moura, D. Botequim, M.G.P.M.S. Neves, S.M.B. Costa, Merging porphyrins with gold nanorods: self assembly construct to high fluorescent polyelectrolyte microcapsules, Nanomaterials 12 (2022) 872–885.